
This is an electronic reprint of the original article.
This reprint may differ from the original in pagination and typographic detail.

Hagen, Dirk; Tripathi, Tripurari; Karppinen, Maarit
Atomic layer deposition of nickel–cobalt spinel thin films

Published in:
Dalton Transactions

DOI:
[10.1039/C7DT00512A](https://doi.org/10.1039/C7DT00512A)

Published: 01/01/2017

Document Version
Peer-reviewed accepted author manuscript, also known as Final accepted manuscript or Post-print

Published under the following license:
Unspecified

Please cite the original version:
Hagen, D., Tripathi, T., & Karppinen, M. (2017). Atomic layer deposition of nickel–cobalt spinel thin films. *Dalton Transactions*, 46(14), 4796–4805. <https://doi.org/10.1039/C7DT00512A>

Cite this: DOI: 10.1039/xxxxxxxxxx

Atomic layer deposition of nickel-cobalt spinel thin films

D. J. Hagen,^a T. S. Tripathi,^a and M. Karppinen^{*a}

Received Date
Accepted Date

DOI: 10.1039/xxxxxxxxxx

www.rsc.org/journalname

We report the atomic layer deposition (ALD) of high-quality crystalline thin films of the spinel-oxide system $(\text{Co}_{1-x}\text{Ni}_x)_3\text{O}_4$. These spinel oxides are ferrimagnetic p-type semiconductors promising for several applications ranging from photovoltaics and spintronics to thermoelectrics. The spinel phase is obtained for Ni contents exceeding the $x = 0.33$ limit for bulk samples. It is observed that the electrical resistivity decreases continuously with x while the magnetic moment increases up to $x = 0.5$. This is in contrast to bulk samples where a decrease of resistivity is not observed for $x > 0.33$ due to the formation of a rock-salt phase. From UV-VIS-NIR absorption measurements, a change from distinct absorption edges for the parent oxide Co_3O_4 to a continuous absorption band ranging deep into the near infrared for $0 < x \leq 0.5$ was observed. The conformal deposition of dense films on high-aspect-ratio patterns is demonstrated.

1 Introduction

Semiconducting oxide thin films form an important class of materials with a number of potential applications such as transparent conductive layers, photocatalysts, thermoelectric generators and battery electrodes.^{1–5} However, the commercial usage of oxide semiconductors has been limited to n-type materials for most of these applications since the electrical conductivity of typical p-type oxides such as CuO , Cu_2O , NiO , CoO and Co_3O_4 is rather low. For most of these materials, this is usually attributed to the localization of holes and the associated Mott-insulator type charge transport by hopping.^{6,7}

An important example where novel p-type metal oxides are particularly desired is oxide thermoelectrics, as for thermoelectric devices it is necessary to combine n- and p-type conductors. Oxide thermoelectrics would be safer and cheaper than the current Bi_2Te_3 based thermoelectric devices; they would also tolerate higher temperatures and harsher conditions, and be more sustainable as they can be prepared of earth-abundant elements.^{8–10} There are relatively efficient thermoelectric materials among simple n-type metal oxides such as ZnO ¹¹ but the quest is for the p-type oxide counterparts.

The spinel $(\text{Co}_{2/3}\text{Ni}_{1/3})_3\text{O}_4$ has attracted increased attention in recent years because it is a p-type semiconductor and possesses relatively high electrical conductivity.^{12–18} Formally, it is an inverse spinel with Ni^{2+} ions occupying the octahedral site (O_h) and Co^{3+} ions distributed over the O_h and tetrahedral site (T_d) but the real cation distribution may significantly differ from this,

depending on the preparation method.¹⁹ The conduction mechanism is still a subject of discussion and a large variation in the resistivity values is reported in literature. For example, Windisch et al.²⁰ reported a room-temperature (RT) resistivity of $0.06 \, \Omega\text{cm}$ for solution deposited films, while they obtained films with a resistivity as low as $0.003 \, \Omega\text{cm}$ by sputtering. Silwal et al.²¹ fabricated epitaxial $(\text{Co}_{2/3}\text{Ni}_{1/3})_3\text{O}_4$ films on MgAl_2O_4 using pulsed laser deposition (PLD) and observed extremely differing electrical properties depending on the growth temperature. They measured RT resistivity values of about $0.001 \, \Omega\text{cm}$ for films deposited at $250 \, ^\circ\text{C}$ and $0.1 \, \Omega\text{cm}$ for films deposited at $600 \, ^\circ\text{C}$. Moreover, the resistivity of the films deposited at high temperatures increased exponentially with decreasing temperature, as it is expected in the case of electrical transport by small polarons, while for the films deposited at low temperatures it decreased over a wide temperature range as it is typical for itinerant charge carriers such as classical holes or large polarons. Similarly, the magnetic nature of $(\text{Co}_{2/3}\text{Ni}_{1/3})_3\text{O}_4$ depends strongly on the deposition method and has been shown to be related to the electrical transport mechanism.^{19,21,22}

Having the eye on the potential applications of semiconducting oxides, atomic layer deposition (ALD) provides us with a number of advantages over other thin-film fabrication techniques. It can be easily scaled up to commercially relevant dimensions and furthermore allows the coating of difficult morphologies and the fabrication of precisely dimensioned heterostructures such as superlattices. For example, our group recently reported the ALD of inorganic-organic superlattices based on the n-type semiconductors ZnO and TiO_2 and demonstrated an increased thermoelectric performance due to a significant decrease of thermal conductivity.

^a Department of Chemistry and Materials Science, Aalto University, Espoo, Finland.
Fax: XX XXXX XXXX; Tel: XX XXXX XXXX; E-mail: maarit.karppinen@aalto.fi

In this work, the ALD of the ternary Ni-Co-oxide system with emphasis on the spinel structure $(\text{Co}_{1-x}\text{Ni}_x)_3\text{O}_4$ ($0 \leq x \leq 1$) is explored and the electrical, thermoelectric, optical and magnetic properties of the films are investigated.

2 Experimental section

The precursors Ni-bis-2,2,6,6-tetramethyl-heptane-3,5-dionate ($\text{Ni}(\text{tmhd})_2$) and Co-bis-2,2,6,6-tetramethyl-heptane-3,5-dionate ($\text{Co}(\text{tmhd})_2$) were synthesized according to literature methods²⁶ and purified by sublimation in vacuum before use. The films were deposited in an ASM-Microchemistry F-120 flow-type reactor which operated under moderate vacuum of 1–3 mbar. We employed metal-tmhd precursors for our ALD process as they are relatively simple to synthesize, are stable in air and can be vaporized at reasonable temperatures. The precursors were placed in open glass boats within the reactor and N_2 was used as a carrier and purging gas. The sublimation temperature for $\text{Co}(\text{tmhd})_2$ was 90 °C and that for $\text{Ni}(\text{tmhd})_2$ 115 °C. Ozone was used as the oxygen source and supplied from a Fischer Modell 502 generator. Mixed oxides were grown by combining subcycles. The term "number of cycles" refers to the total number of subcycles in this work and 2400 cycles were used except where declared otherwise.

The thickness of the films was determined by X-ray reflectivity (XRR) measurements using a Panalytical X'Pert Pro MPD diffractometer with Cu K- α radiation. The same instrument was also used for grazing-incidence X-ray diffraction (GIXRD) with an incidence angle $\omega = 0.5^\circ$, a step size of 0.025° and a time per step of 10 s for the identification of crystalline phases. The crystal structures were further investigated using a JEOL JEM-2200FS double aberration corrected transmission electron microscope, equipped with a Schottky field emission gun (FEG) and operated at an accelerating voltage of 200 kV. Cross-sections of the films were prepared using a focused ion beam (FIB). Furthermore, the chemical composition of the cross-section was explored with a JEOL lithium-drifted silicon (Si-Li) energy dispersive X-ray spectrometer and by electron energy loss spectroscopy (EELS) using an in-column OMEGA-type energy filter.

The optical properties were evaluated by absorption spectroscopy using a Hitachi U-2000 Spectrophotometer. Raman spectra were recorded with a LABRAM HR instrument using an helium-neon laser at a wavelength of 632.8 nm.

The sheet resistance of the samples was measured with an Jandel RM3000 four probe test unit. The temperature dependence of the resistivity was measured with a home-built setup in a linear four-probe configuration. The Seebeck coefficient (S) was determined using a home-made setup (described in²⁷) based upon an equilibrium measurement technique. The magnetic moment at various temperatures was measured with the physical property measurement system (PPMS) Dynacool (Quantum Design, Inc.) using vibrating sample magnetometry (VSM).

3 Results and discussion

We first investigated the growth of the binary Co oxide by varying the $\text{Co}(\text{tmhd})_2$ pulse length at a temperature of 200 °C keeping the O_3 pulse length at 3 s. As can be seen in Figure 1 where

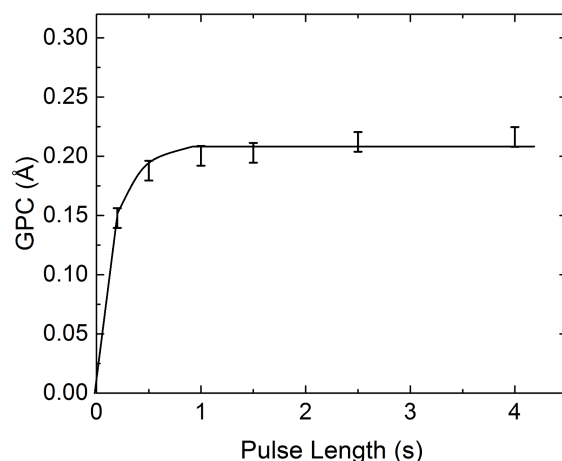


Fig. 1 GPC as a function of $\text{Co}(\text{tmhd})_2$ pulse length for a Co_3O_4 film at a deposition temperature of 200 °C for a fixed O_3 pulse length of 3 s.

the growth per cycle (GPC) is plotted against the pulse length, the growth saturates already for relatively short pulse times of 1 s at a rate of 0.2 Å/cycle which is similar to the results reported by Klepper et al.²⁸ When NiO films were grown using a precursor pulse length of 2.5 s and a precursor sublimation temperature of 115 °C a similar GPC value of about 0.2 Å/cycle was measured. Therefore, we chose the growth conditions for the ternary Ni-Co-oxide films as follows: 1s $\text{Co}(\text{tmhd})_2$ pulses followed by 2s purges and 2.5s $\text{Ni}(\text{tmhd})_2$ pulses followed by 3s purges. The O_3 pulse length was 3s followed by a 5s purge for both subcycles, and a supercycle consisted of Ni and Co subcycles with the ratio $\text{Ni}/(\text{Ni}+\text{Co})=x$. Within a supercycle, the subcycles were adequately mixed to avoid the formation of films consisting of separate layers. The deposition temperature of 200 °C was retained in this work as it is well above the vaporization temperatures and below the decomposition temperatures of the precursors.

All our as-deposited thin films were crystalline. This is often not the case for multi-metal-oxide thin films grown by ALD^{29,30} including the eponym material for the spinel structure MgAl_2O_4 ³¹, but in line with the in-situ crystallization observed by Coll et al.³² for Co_2FeO_4 and Uusi-Esko et al.³³ for Co_2MnO_4 . Figure 2 shows GIXRD patterns for our $(\text{Co}_{1-x}\text{Ni}_x)_3\text{O}_4$ films within the whole substitution range x . For pure Co-oxide, the characteristic peaks of the spinel Co_3O_4 can be clearly identified, while the pure Ni-oxide film crystallizes to the rock-salt-structured NiO. Within $0 \leq x \leq 0.33$ the films are clearly of the spinel phase, and for $0.75 \leq x \leq 1$ of the $(\text{Ni},\text{Co})\text{O}$ phase. When the Ni content in the spinel phase increases, only a slight shift of the peaks can be observed as expected since the lattice parameters of Co_3O_4 and $(\text{Co}_{2/3}\text{Ni}_{1/3})_3\text{O}_4$ spinel phases are very close. Similarly, the peak positions for the $x = 0.75$ and the NiO films are nearly identical. In the $x = 0.66$ film, both types of phases, spinel and rock-salt, appear to be present as can be seen from the double peak between 34 and 39° and the peaks at 44.2 and 64.3° which are most likely superpositions of the spinel 400 and the rock-salt 200 respectively the 440 and 220 diffractions. The most interesting pattern is that

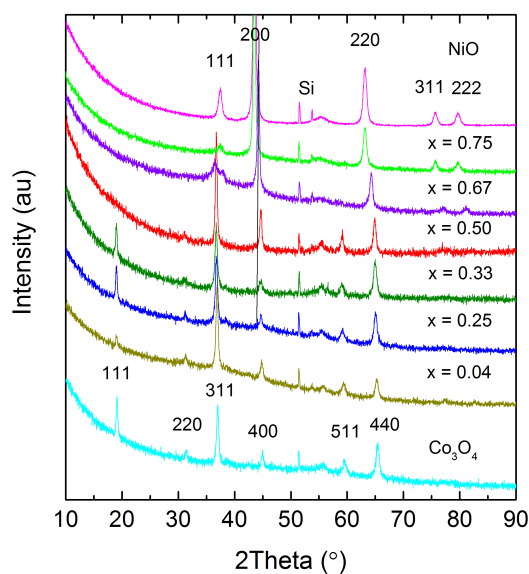


Fig. 2 XRD patterns of $(\text{Co}_{1-x}\text{Ni}_x)_3\text{O}_4$ films with different Ni contents x . The Miller indices are for the parent oxides, Co_3O_4 and NiO .

for the $x = 0.5$ film. The 220, 311, 511 and 440 peaks of the spinel phase are clearly present showing that it is still the dominant phase at this high x value. The disappearance of the 111 peak is most likely due to the extreme sensitivity of the 111 diffraction to the exact ion distribution within a spinel³⁴ and a very low intensity of this diffraction peak is also observed for the $x = 0.04$ film. The relative height of the peak at 44.6° is much larger than for the film with lower x indicating that some rock-salt phase might already be present. Nevertheless, the dominance of the spinel peak is a remarkable result since this is clearly beyond the stoichiometric composition $x = 0.33$ which has been reported to be the solubility limit for bulk material prepared by high-pressure sintering³⁵ and for samples fabricated by solution-based methods.²⁰ The possibility of obtaining $(\text{Ni}_x\text{Co}_{1-x})_3\text{O}_4$ with a high Ni content x was however also reported by Windisch et al.²⁰ for sputtered films. The lattice parameters of the spinel phase films were estimated from the 311 diffraction peak. For the $x = 0$ film, a value of 8.05 \AA was calculated which is close to the value of 8.065 \AA measured by Roth³⁶ for bulk samples. The lattice parameter increases to 8.08 \AA for $x = 0.04$, 8.11 \AA for $x = 0.25$ and 8.12 \AA for $x = 0.33$. For $x = 0.5$, a lattice parameter of 8.11 \AA was determined. An increase of the lattice parameter with x was also observed by Appandairajan and Gopalakrishnan³⁷ and explained by the fact that the ionic radius of Ni^{2+} ions is larger than that of low-spin Co^{3+} ions. It is important to note that the analysis of the diffraction patterns is much more complicated for thin films measured with GIXRD than for bulk samples measured in Bragg-Brentano symmetry. One indication for this difficulty is the change of the full half-width of maximum (FWHM) of the peaks with scattering angle^{38,39} as can be seen for example for the spinel-phase 111 and 440 peaks in Figure 2.

The structure of the films was investigated with transmission electron microscopy (TEM) (Figure 3). The films are rather smooth and consist of small grains. Unfortunately, the cross-

section contains a superposition of many grains in a row which makes it difficult to analyze the size distribution quantitatively. However, it can be seen that the typical grain size is in the nanometer range. From the selected-area electron diffraction pattern in Figure 3, the random distribution of grain orientations is evident, even though the pattern is far from the continuous rings which are expected for grains much smaller than the sampling area. An elemental-composition profile along the cross-section was obtained with energy-dispersive X-ray spectroscopy (EDS). As can be seen in Figure 3, the Co/Ni ratio is quite constant across the film and close to the expected value. Furthermore, the C content is below the detection limit of EDS.

The ratio of the EELS L_2 and L_3 peak intensities has been used to determine the mean oxidation state of metal cations including Co.^{40,41} In short, the inelastic scattering of electrons is mainly caused by the excitation of inner-shell electrons (2p for the first-row transition metals) to the continuum and higher electronic states (mainly the 3d states for the first-row transition metals). The excitation to the continuum results in a double-step function with a step ratio of 2/1 due to the occupation of the $2p_{1/2}$ and $2p_{3/2}$ states. The excitation to the 3d states leads to characteristic peaks, whose ratio usually differs from 2:1 and depends on the oxidation state. The reason for this is still a subject of discussion. According to Wang et al.,⁴⁰ a L_3/L_2 intensity ratio of ca. 4.8 is expected for Co^{2+} while ca. 3.3 is expected for $\text{Co}^{2.67+}$ as it is present in Co_3O_4 . For Co^{3+} in a completely inverse spinel $(\text{Co}_{2/3}\text{Ni}_{1/3})_3\text{O}_4$, even lower values would be expected. From the EELS scan in Figure 4, a ratio of 3.5 was determined after subtraction of the background showing that the mean oxidation state of Co is smaller than +3. It is understood that the cation distribution can differ significantly from the ideal inverse spinel and varies with the preparation conditions leading to a broad variation of electric and magnetic properties. For example, while Iliev et al.⁴² obtained a distribution close to that of the ideal inverse spinel for their insulating $(\text{Co}_{2/3}\text{Ni}_{1/3})_3\text{O}_4$ films from Raman analysis, the results for the conducting, metal-like films suggested a distribution differing from that. Bitla et al.¹⁹ who investigated similar films (epitaxial, on MgAl_2O_4) carried out extensive investigations of the cation distribution by X-ray absorption spectroscopy (XAS) and obtained $(\text{Co}_{0.54}^{2+}\text{Co}_{0.46}^{3+})[\text{Ni}_{0.62}^{2+}\text{Ni}_{0.38}^{3+}\text{Co}_{0.05}^{2+}\text{Co}_{0.95}^{3+}]\text{O}_4$ for metal-like films and $(\text{Co}_{0.54}^{2+}\text{Co}_{0.46}^{3+})[\text{Ni}_{0.82}^{2+}\text{Ni}_{0.28}^{3+}\text{Co}_{0.13}^{2+}\text{Co}_{0.87}^{3+}]\text{O}_4$ for an insulating film referring to effective Co oxidation numbers of +2.71 and +2.66, respectively. Our results confirm the deviation from the ideal inverse spinel structure and suggest oxidation states similar to that reported by Bitla and co-workers.

Raman spectra for our $(\text{Co}_{1-x}\text{Ni}_x)_3\text{O}_4$ films are shown in Figure 5. For the parent Co_3O_4 film, peaks are clearly visible at 195, 481, 621 and 690 cm^{-1} , which correspond to the modes F_{2g} , E_g , F_{2g} and A_{1g} , respectively.⁴³ Another F_{2g} would be expected at about 522 cm^{-1} but cannot be identified here due to the interference with a signal from Si. When Ni is added, the intensity of the peaks decreases dramatically, its width increases and the A_{1g} peak that is usually assumed to be dominated by the O_h oxygen atoms⁴⁴ shifts to lower wavenumbers. This is similar to the observations which Windisch et al.⁴⁴ made for solution-deposited $(\text{Co}_{1-x}\text{Ni}_x)_3\text{O}_4$ films. The energy shift was explained with the

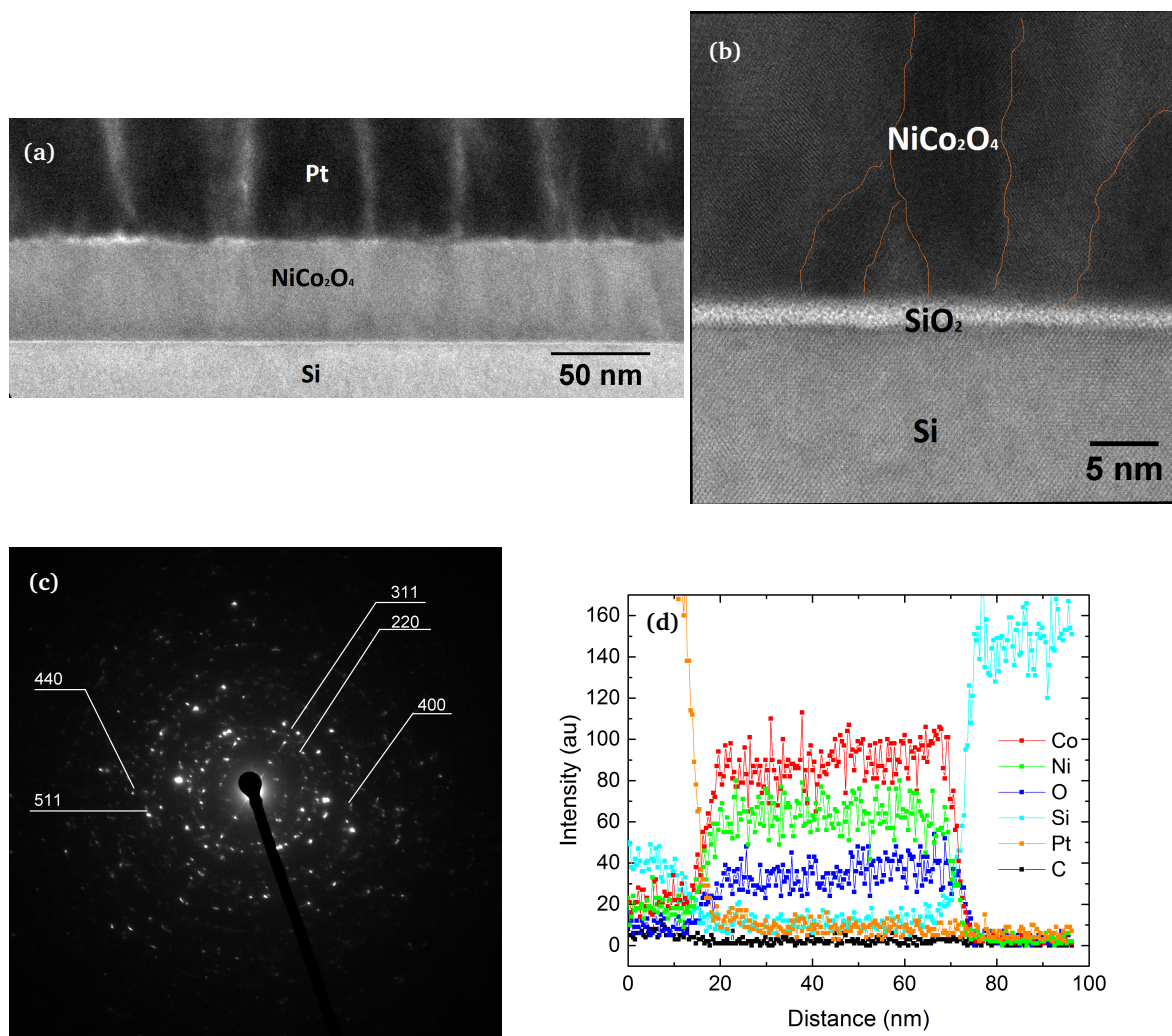


Fig. 3 TEM analysis of a representative $(\text{Co}_{1-x}\text{Ni}_x)_3\text{O}_4$ film ($x = 0.33$): (a) low-magnification image, (b) high-magnification image (some grain boundaries are indicated), (c) selected-area electron diffraction pattern, (d) elemental profile measured with EDS.

replacement of Co^{3+} by Ni^{2+} ions and the decrease in peak intensity and increase of bandwidth with the related decrease of symmetry at the O_h site.⁴⁴ In order to demonstrate the presence of weak Raman peaks in the stoichiometric $(\text{Co}_{1-x}\text{Ni}_x)_3\text{O}_4$ films with $x=0.33$, an inset with the Raman spectrum of a thicker film (~ 192 nm) is included in Figure 5. Iliev et al.⁴² also observed weak and broad peaks for their metallic films grown at low temperatures but obtained sharp peaks for their insulating films grown at high temperatures during their epitaxy studies supporting the idea that ionic disorder is responsible for the low resistivity.

The electrical resistivity of films of varying composition is shown in Figure 6. It can clearly be seen that films of low Ni contents, which one might call Ni-doped, have already significantly lower resistivities than the pure Co_3O_4 . The sheet resistivity decreases beyond the stoichiometric $x = 0.33$ composition, for which a resistivity of $0.0014 \, \Omega\text{cm}$ was measured. When a NiO phase crystallizes the resistivity increases drastically and reaches values beyond the measurement range of our set-up ($\sim \text{M}\Omega/\text{sq}$)

already at the Ni concentration of $x = 0.75$.

One explanation for the doping effects of Ni ions on Co_3O_4 was provided by Perkins et al.⁴⁵ They argued that Ni^{2+} ions replacing Co^{3+} ions on the O_h site would represent electron acceptors, and therefore hole sources. The inverse spinel $(\text{Co}_{2/3}\text{Ni}_{1/3})_3\text{O}_4$ was described as an end point of Ni alloying. However, since a conversion from the normal spinel Co_3O_4 to the mainly inverse spinel $(\text{Co}_{2/3}\text{Ni}_{1/3})_3\text{O}_4$ is expected, a simple ion replacement is not a sufficient model and larger rearrangements have to be taken into account. Furthermore, the ionic radii of Ni^{2+} and low-spin Co^{3+} differ significantly (83 pm vs 68.5 pm).⁴⁶

The exact charge transport mechanism in $(\text{Co}_{2/3}\text{Ni}_{1/3})_3\text{O}_4$ has been a subject to intensive debate. From the increase of conductivity with increasing Ni content it was proposed that the conduction proceeds via the hopping of holes between octahedral Ni ions. Bitla et al.¹⁹ investigated the band structure and the conduction mechanisms of their epitaxial PLD-grown $(\text{Co}_{2/3}\text{Ni}_{1/3})_3\text{O}_4$ films extensively. They argued that a ferromagnetic double-exchange interactions between adjacent octahedral

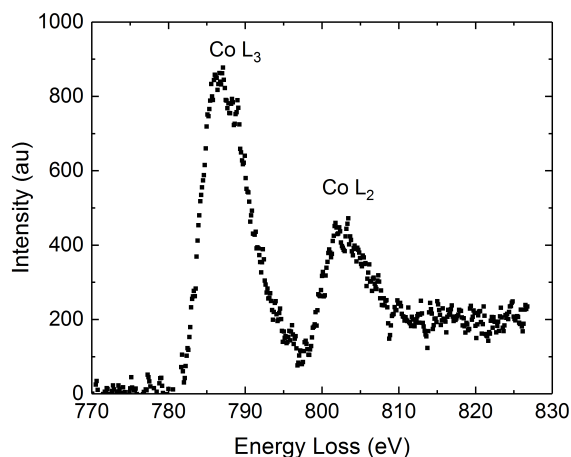


Fig. 4 EELS graph for the $(\text{Co}_{1-x}\text{Ni}_x)_3\text{O}_4$ film with $x=0.33$: the ratio of the Co L3 and L2 peaks strongly indicates a valence lower than +3.

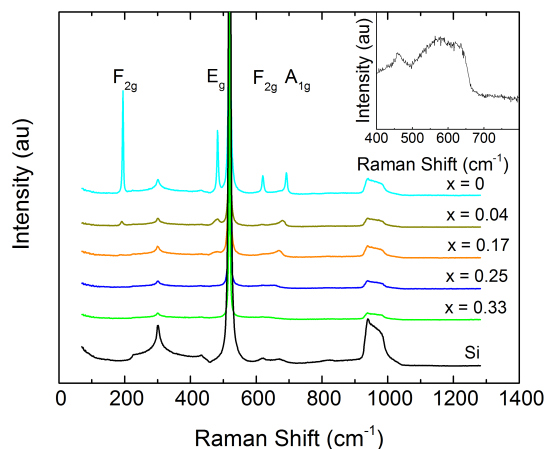


Fig. 5 Raman spectra for $(\text{Co}_{1-x}\text{Ni}_x)_3\text{O}_4$ films with different Ni contents x . The inset shows the Raman spectrum for a film with $x = 0.33$ and a thickness of 192 nm in higher resolution.

Ni^{3+} and Ni^{2+} species exists which is accompanied by strong delocalization of charge carriers leading to high conductivities. Furthermore, they observed an increase of resistivity with temperature, as it is typical for itinerant charge carriers, over a wide temperature range, and a transition to an opposite temperature dependency. Since this metal-insulator transition was typically close to the Curie temperature, they concluded the occurrence of magnetic polarons. Similar observations were also made by Silwal et al.²¹ However, small-polaron formation due to the interaction with phonons and disappearance of the activation energy at low temperatures is a typical observation for oxides⁴⁷ and could be an alternative explanation.

Figure 6 shows the change of resistance with temperature for our $(\text{Co}_{1-x}\text{Ni}_x)_3\text{O}_4$ films of varying composition. The absolute resistance of the Co_3O_4 film reaches 1 M Ω at about 220 K and 10 M Ω at about 160 K exceeding the measurement range of our

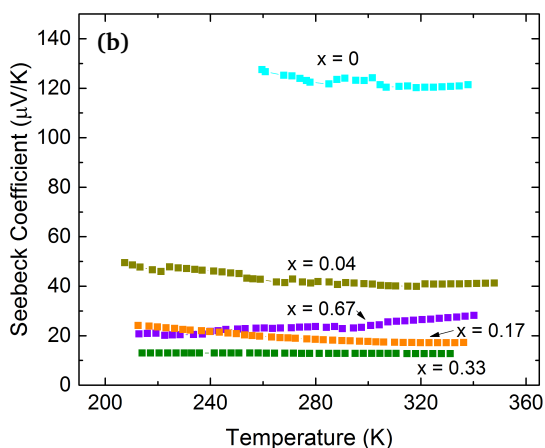
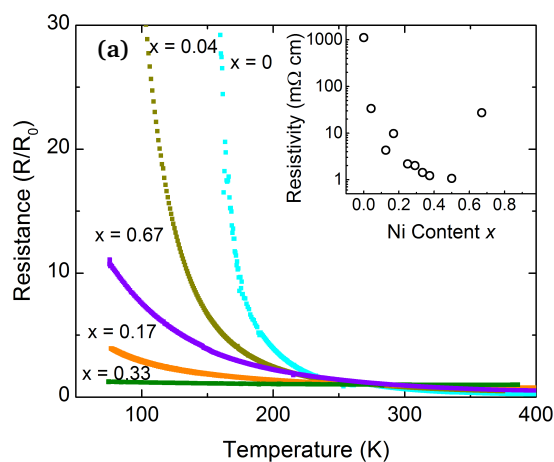


Fig. 6 Thermoelectric properties of $(\text{Co}_{1-x}\text{Ni}_x)_3\text{O}_4$ films: (a) resistance change with temperature; the resistance has been normalized to the value measured at 273 K. The inset shows the RT resistivity values depending on the Ni content x . (b) Temperature dependence of the Seebeck coefficient.

setup. For the stoichiometric $x = 0.33$ film, the resistance decreases with temperature over the whole temperature range as it is expected for polaron hopping. This is in contrast to the observations of Bitla et al.¹⁹ and Silwal et al.²¹ despite the resistivity of 0.0014 Ωcm is similar to the values these groups obtained for their 'metallic' $(\text{Co}_{2/3}\text{Ni}_{1/3})_3\text{O}_4$ films. One possible explanation for this is the polycrystalline nature of the films. If the grain size is smaller than the mean free path of charge carriers, the scattering at grain boundaries becomes dominant over the scattering by phonons. Further scattering centers include point defects. Thus, even if delocalized charge carriers were present, no decrease of resistivity with decreasing temperature might be observed. However, the temperature dependence of the resistivity is quite low and it has already been described in the early research on polarons that the temperature dependence of electrical resistance can change from positive to negative for the transport by large

polarons if lattice defects are present.⁴⁷ For films with small Ni content x or mixed phases (i.e. $x = 0.67$), the increase of resistance with decreasing temperature is much higher which shows higher activation energies for the charge transport. Nevertheless, it is apparent that even very small contents of Ni have a strong impact on the electrical properties and decrease both the absolute resistance values and the resistance change with temperature.

Typically, the electrical transport by small-polaron hopping is described by an exponential equation in the form of^{48–50}:

$$\rho = \rho_0 T^\gamma \exp\left(\frac{T_0}{T}\right)^p, \quad (1)$$

where ρ is the electrical resistivity, ρ_0 a pre-exponential factor and T_0 a characteristic temperature of the material. A lower value for T_0 corresponds to a lower activation energy for the charge-carrier transport. The parameters γ and p differ for the different hopping models with $\gamma = p = 1$ for nearest-neighbor hopping, $\gamma = 0.5$ and $p = 0.25$ for the variable-range hopping model of Mott, and $\gamma = 1$ and $p = 0.5$ for the variable range hopping model of Efros and Shklovskii. The difference between the two variable-range hopping models is the distribution of states around the Fermi-level and the way how the Coulomb interaction between localized charge carriers is considered. Plotting $\ln(R/(R_0 T^{0.5}))$ versus $1/T^{0.25}$, one can see that the temperature dependencies fit quite well to Mott's equation and obtain characteristic temperatures T_0 of 5.8×10^7 K for $x = 0$, 9.4×10^6 K for $x = 0.04$, 2.6×10^5 K for $x = 0.17$, 8.0×10^3 K and 2.3×10^4 K for $x = 0.50$. This significant decrease of T_0 , and thus of the activation energy, indicates a fundamental change of the charge transport mechanism.

In Figure 6, the temperature dependence of the Seebeck coefficient of different $(\text{Co}_{1-x}\text{Ni}_x)_3\text{O}_4$ films is shown. The trend is quite consistent with that of the resistance and the Seebeck coefficient decreases from the high RT value of $\sim 120 \mu\text{V/K}$ for pure Co_3O_4 to values between 10 and $20 \mu\text{V/K}$ for the Ni-substituted films. In spite of this decrease, the thermoelectric power factor S^2/ρ , which is a measure for the electronic contribution to the quality of a thermoelectric material, increases from a value of $1.4 \times 10^6 \mu\text{V}^2/(\text{K}^2\Omega\text{m})$ for the parent Co_3O_4 compound to $15.6 \times 10^6 \mu\text{V}^2/(\text{K}^2\Omega\text{m})$ for a film with $x = 0.5$. For most films, a rather small decrease of S with increasing temperature is observed which is in agreement with the resistance measurements. In contrast, an increase of the Seebeck coefficient was measured for films with $x = 0.67$. This is rather uncommon as its resistance decreases with temperature. However, the film consists of more than one phase, spinel and rock-salt-type NiO, thus the conduction mechanism can be quite complicated for multi-phase systems.

Optical absorption data of films with varying composition are shown in Figure 7. The most remarkable observation is the increase of absorption at longer wavelengths, thus right of the characteristic peaks, when Ni is added to Co_3O_4 . Such an absorption can usually be attributed to plasmons and the increase of absorption with increasing Ni content is a strong indication for an increasingly metallic character of the films. Furthermore, the two characteristic absorption peaks of Co_3O_4 vanish within the broad absorption band with increasing Ni content. There exist

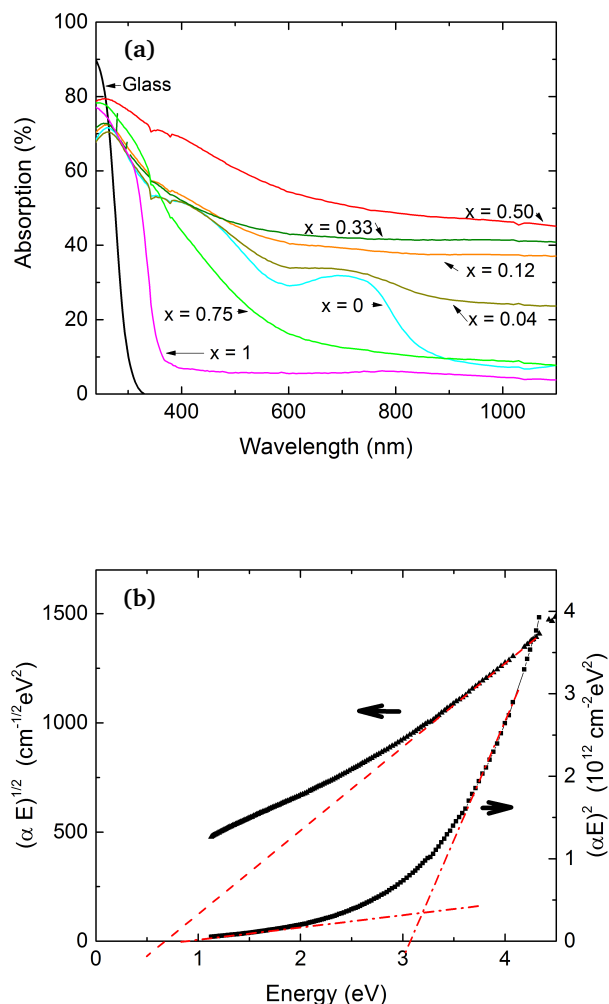


Fig. 7 UV-VIS-NIR absorption spectra: (a) absorption as a function of wavelength for $(\text{Co}_{1-x}\text{Ni}_x)_3\text{O}_4$ films with varying Ni content x ; (b) $(\alpha E)^2$ - E and $(\alpha E)^{1/2}$ - E characteristic for a film with $x = 0.33$.

different approaches for obtaining information on the band gap from absorption spectra and two very common are plotting $(\alpha E)^2$ and $(\alpha E)^{1/2}$ versus E in order to estimate direct and indirect bandgaps, respectively.⁵¹ Here, α is the absorption coefficient, which is calculated as $\alpha = \ln((1 - R)(1 - A_{\text{Gl}})/T)/d$, where R is the reflectance, A_{Gl} the absorption of the borosilicate-glass substrate, T the transmission and d the film thickness, and E is the photon energy. For Co_3O_4 , direct bandgaps at 1.5 and 2.1 eV, and indirect band gaps at 1.2 and 1.3 eV can be identified for the two main absorption peaks. Furthermore, there are indications for an indirect transition at 0.6 eV. Quiao et al.⁵² interpreted the low-energy peak as d-d transitions from the O_h Co ions and the high energy peak to the charge transfer from oxygen anions. The lowest-energy transition was identified to occur between d electrons of the T_d Co ions. The peaks are still clearly visible for a small Ni content of $x = 0.04$ and direct bandgaps of 1.3 and 2.1 eV and indirect band gaps of 0.7 and 0.9 eV can be obtained. For

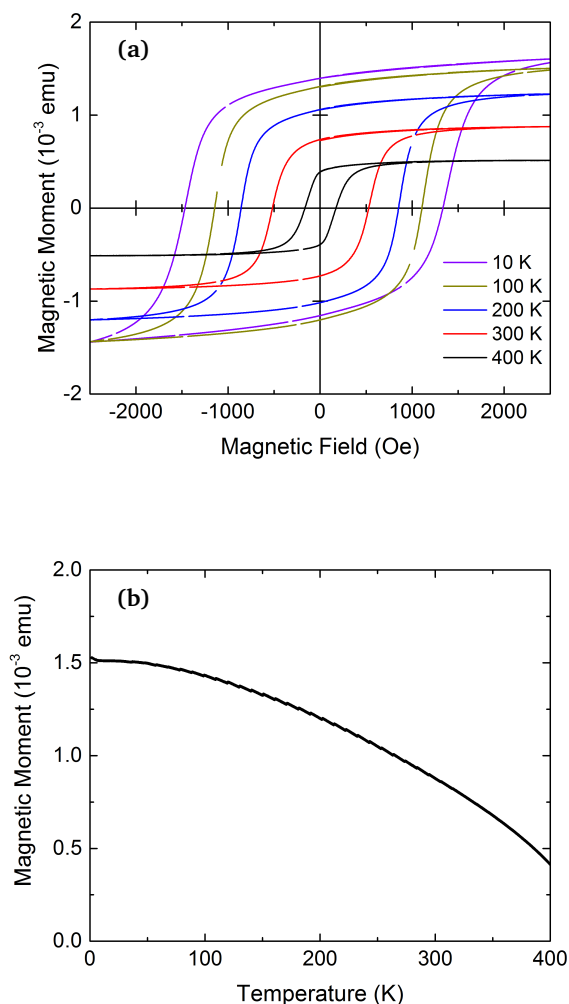


Fig. 8 Magnetic characterization of a $(\text{Co}_{1-x}\text{Ni}_x)_3\text{O}_4$ film with $x = 0.33$ (deposited with 9600 cycles): (a) saturation curves at various temperatures; (b) magnetic moment vs temperature under a field of 2000 Oe.

higher Ni contents, the analysis becomes more difficult as can be seen from the example of a film with $x = 0.33$ in Figure 7. A direct bandgap above 3 eV might be attributed to charge transfer between oxygen ions and higher vacant metal orbitals.⁵² From the low-energy part of the direct-bandgap curve one can derive a bandgap slightly higher than 1 eV which might indicate similar d-d transition energies for the ions on the O_h site as in Co_3O_4 . Fitting the indirect-bandgap curve yields a value of 0.67 eV which appears realistic for a d-d transition on the T_d site. Bitla et al.¹⁹ reported direct bandgaps of 3.9 and 2.64 eV for their metallic epitaxial $(\text{Co}_{2/3}\text{Ni}_{1/3})_3\text{O}_4$ films while Dileep et al.⁵³ measured direct band gaps of 1.84, 2.76, and 3.29 eV and indirect band gaps of 0.38 and 1.42 eV for epitaxial $(\text{Co}_{2/3}\text{Ni}_{1/3})_3\text{O}_4$ films using EELS. However, both authors reported a significant variation of the band gap values depending on the preparation method. For our films, we observed a shift of the high-energy direct bandgap with increasing Ni content from 3.51 eV for $x = 0.04$ to 3.33 eV

for $x = 0.12$, 3.08 eV for $x = 0.33$ and 2.99 eV for $x = 0.5$.

The magnetic properties of $(\text{Co}_{2/3}\text{Ni}_{1/3})_3\text{O}_4$ are of great interest and significantly varying magnetic moments per unit cell have been reported since the distribution of the metal ions (Co^{2+} , Co^{3+} , Ni^{2+} , Ni^{3+}) varies strongly with the deposition process.^{14,19,21,22,53–55} Most often, $(\text{Co}_{2/3}\text{Ni}_{1/3})_3\text{O}_4$ is described as ferrimagnetic resulting from superexchange between Ni ions on the O_h site and Co ions on the T_d site.⁵⁴ However, the various ionic species possible in this material result in many different exchange pairs with negative as well as positive interactions. For example, ferromagnetic double-exchange is expected between O_h Ni^{+2} and Ni^{+3} species.¹⁹ In order to explore the magnetic properties of our ALD $(\text{Co}_{2/3}\text{Ni}_{1/3})_3\text{O}_4$, 9600 cycles were used to deposit thicker films of about 192 nm. As can be seen in Figure 8, magnetic hysteresis was still observed at 400 K, which was the highest temperature available in our set up. This is in agreement with a critical temperature of 673 K^{19,56} for the bulk material, although lower values were reported for thin films.^{19,21} At low

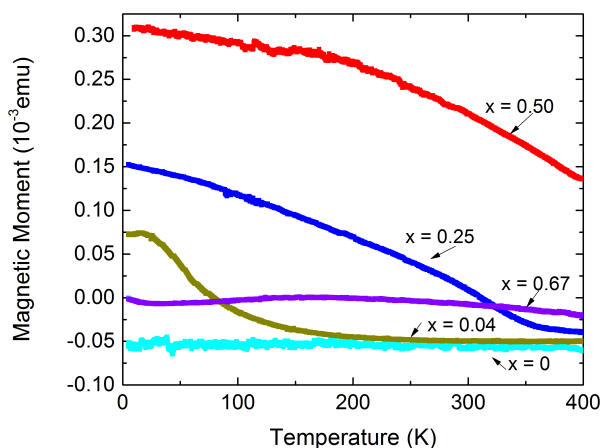


Fig. 9 Magnetic moment vs temperature at a field of 10 kOe for $(\text{Co}_{1-x}\text{Ni}_x)_3\text{O}_4$ films with different Ni contents x . The dielectric background has not been subtracted.

temperatures, the saturation magnetization reaches a value of about 0.0015 emu and a high coercive field of about 1.3 kOe. Estimating the amount of material from the sample thickness and area ($\sim 10.5 \times 4.5 \text{ mm}^2$), one obtains a magnetic moment of $1.2 \mu_B$ per unit cell. This is less than the value of $2 \mu_B$ expected for a fully inverse spinel NiCo_2O_4 (assuming high-spin Co^{3+} on the T_d site and low-spin Co^{3+} on the O_h site) but on a realistic order of magnitude taking into account the results by other groups.^{53–55,57} Dileep et al. explained the low magnetic moment with the transfer of charges between the ionic sites.⁵³ The temperature-dependent magnetic moments of films with varying Ni content are shown in Figure 9. The films were grown with 2400 cycles at 200°C and the measurements were performed at an applied magnetic field of 10 kOe. It can be clearly seen that both the magnetization and the critical temperature increase with the Ni content (and also the coercivity which is not shown here). Furthermore, even small contents of Ni are suf-

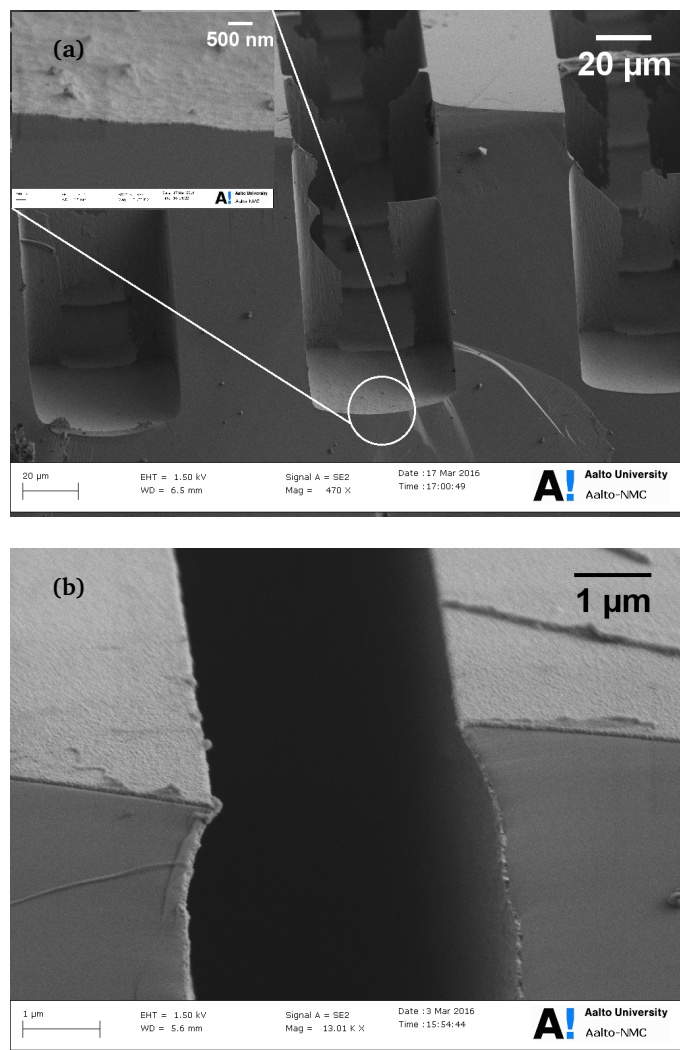


Fig. 10 SEM micrographs of trenches coated with $(\text{Co}_{1-x}\text{Ni}_x)_3\text{O}_4$ ($x = 0.33$): (a) typical trenches, the inset shows the film on the trench bottom, (b) film on top of a narrow trench

ficient to change the antiferromagnetic Co_3O_4 into a compound with a sizable positive magnetic moment. The strong effect of the Ni content on both the electric and magnetic properties indicates a correlation of both properties and supports the model of Bitla et al.¹⁹ who suggested that the magnetic properties of metallic, epitaxial $(\text{Co}_{2/3}\text{Ni}_{1/3})_3\text{O}_4$ are dominated by ferromagnetic double-exchange interaction of Ni^{2+} and Ni^{3+} species on octahedral sites and that this double-exchange is also responsible for the metallic conduction characteristic observed by them. However, direct interaction of Ni cations on adjacent O_h sites might also be taken into account for a complete description^{58,59} since the distance between them is much smaller for the $(\text{Co}_{1-x}\text{Ni}_x)_3\text{O}_4$ films (e.g. 2.87 Å for $x = 0.33$) than for the NiO films (~ 2.94 Å). For high Ni contents outside the spinel region, the magnetic properties are difficult to interpret as can be seen in Figure 9 for a film with $x = 0.67$. Here an interplay between a ferromagnetic $(\text{Co}_{1-x}\text{Ni}_x)_3\text{O}_4$ and an antiferromagnetic NiO phase seems to exist.

Finally, we like to emphasize that the high conductivity of the low temperature processed films as well as the possibility to deposit films with Ni contents higher than that of stoichiometric $(\text{Co}_{2/3}\text{Ni}_{1/3})_3\text{O}_4$ are advantages of gas-phase deposition methods as compared to solution-based techniques. Moreover the use of ALD opens the possibilities for the fabrication of nano-structures which are difficult to obtain with other low-temperature deposition techniques such as physical vapor deposition (PVD). Figure 10 shows SEM micrographs of a $(\text{Co}_{1-x}\text{Ni}_x)_3\text{O}_4$ film with $x = 0.33$ deposited on a trenched substrate with 2400 cycles. For the deposition of this film longer pulse and purge times were used (5 s $\text{Co}(\text{thmd})_2$, 6 s $\text{Ni}(\text{thmd})_2$, 5 s O_3 , 8 s purge after metal precursors, 10 s purge after O_3). The high conformality across the trenches demonstrates the suitability of this ALD process.

4 Conclusions

High-quality ternary oxide $(\text{Co}_{1-x}\text{Ni}_x)_3\text{O}_4$ thin films spanning the whole composition range between Co_3O_4 and NiO were deposited by ALD for the first time. For films with Ni/(Co+Ni) ratios x ranging from 0 to 0.5, the dominant phase was of spinel type as proven by XRD while only for the higher Ni contents NiO was formed. This is an advantage compared to bulk material for which the rock-salt structure is dominant for $x > 0.33$. Within the spinel-type region, electrical resistivity decreases with increasing Ni content. The resistivities of spinel films with Co contents of the stoichiometric composition $(\text{Co}_{2/3}\text{Ni}_{1/3})_3\text{O}_4$ (0.0014 Ωcm) and less (0.00107 Ωcm) were much lower than that of bulk $(\text{Co}_{2/3}\text{Ni}_{1/3})_3\text{O}_4$ and comparable to $(\text{Co}_{2/3}\text{Ni}_{1/3})_3\text{O}_4$ films prepared by PVD (0.003 Ωcm, Windisch et al.²⁰) and laser-ablation epitaxy (0.00083 Ωcm, Bitla et al.¹⁹). These low resistivities increase the thermoelectric power factor of Co_3O_4 overcompensating the decrease of the Seebeck coefficient due to the doping.

The decrease in electrical resistivity is accompanied with an increase in the magnetic saturation moment, coercivity and critical temperature. This supports the model that the ferromagnetic double-exchange involving octahedral Ni^{3+} ions is the mechanism that dominates the electrical and magnetic properties. The delocalization of charge carriers and the associated increased metallic character of the films was also confirmed by optical ab-

sorption measurements. Furthermore, the deposition onto high-aspect ratio structures was demonstrated. This is a key advantage of ALD compared to other thin-film deposition techniques such as PVD and enables the usage of $(\text{Co}_{1-x}\text{Ni}_x)_3\text{O}_4$ films in nanostructures such as multi-layer nanotubes in future research.

Acknowledgement

The present work has received funding from the European Research Council under the European Union's Seventh Framework Programme (FP/2007-2013)/ERC Advanced Grant Agreement (No. 339478) and also from the Academy of Finland (Nos. 292431 and 303452). Part of this research has been conducted at OtaNano facilities of Aalto University. We would like to thank Dr Hua Jiang for conducting the TEM analysis.

References

- 1 X. Yu, T. J. Marks and A. Facchetti, *Nature Mater.*, 2016, **15**, 383 – 396.
- 2 K. Ellmer, *Nature Phot.*, 2012, **6**, 809 – 817.
- 3 A. Stadler, *Materials*, 2012, **5**, 661 – 683.
- 4 J. Meyer, S. Hamwi, M. Kröger, W. Kowalsky, T. Riedl and A. Kahn, *Adv. Mater.*, 2012, **24**, 5408 – 5427.
- 5 M. V. Reddy, G. V. S. Rao and B. V. R. Chowdari, *Chem. Rev.*, 2013, **113**, 5364 – 5457.
- 6 V. I. Anisimov, M. A. Korotin and E. Z. Kurmaev, *J. Phys.: Condens. Matter*, 1990, **2**, 3973 – 3987.
- 7 J. Hugel and C. Carabatos, *J. Phys. C: Solid State Phys.*, 1983, **16**, 6713 – 6721.
- 8 K. Koumoto, Y. Wang, R. Zhang, A. Kosuga, and R. Funahashi, *Annu. Rev. Mater. Res.*, 2010, **40**, 363 – 394.
- 9 J. He, Y. Liu and R. Funahashi, *J. Mater. Res.*, 2011, **26**, 1762 – 1772.
- 10 G. Ren, J. Lan, C. Zeng, Y. Liu, B. Zhan, S. Butt, Y.-H. Lin and C.-W. Nan, *JOM*, 2015, **67**, 211 – 221.
- 11 T. Tsubota, M. Ohtaki, K. Eguchi and H. Arai, *J. Mater. Chem.*, 1997, **7**, 85 – 90.
- 12 B. Cui, H. Lin, Y.-Z. Liu, J.-B. Li, P. Sun, X.-C. Zhao and C.-J. Liu, *J. Phys. Chem. C*, 2009, **113**, 14083 – 14087.
- 13 L. Hu, L. Wu, M. Liao, X. Hu and X. Fang, *Adv. Funct. Mater.*, 2012, **22**, 998 – 1004.
- 14 F. Iacomi, G. Calin, C. Scarlat, M. Irimia, C. Doroftei, M. Dobromir, G. Rusu, N. Iftimie and A. Sandu, *Thin Solid Films*, 2011, **520**, 651 – 655.
- 15 T. Li, X. Li, Z. Wang, H. Guo and Y. Li, *J. Mater. Chem. A*, 2015, **3**, 11970 – 11975.
- 16 N. Padmanathan and S. Selladurai, *RSC Adv.*, 2014, **4**, 8341 – 8349.
- 17 Z. Wu, Y. Zhu and X. Ji, *J. Mater. Chem. A*, 2014, **2**, 14759 – 14772.
- 18 G. Zhang and X. W. D. Lou, *Adv. Mater.*, 2013, **25**, 976 – 979.
- 19 Y. Bitla, Y.-Y. Chin, J.-C. Lin, C. N. Van, R. Liu, Y. Zhu, H.-J. Liu, Q. Zhan, H.-J. Lin, C.-T. Chen, Y.-H. Chu and Q. He, *Sci. Rep.*, 2015, **5**, 15201.
- 20 C. F. Windisch, Jr., G. J. Exarhos, K. F. Ferris, M. H. Engelhard and D. C. Stewart, *Thin Solid Films*, 2001, **398 - 399**, 45 – 52.
- 21 P. Silwal, L. Miao, I. Stern, X. Zhou, J. Hu and D. H. Kim, *Appl. Phys. Lett.*, 2012, **100**, 032102.
- 22 P. Silwal, L. Miao, J. Hu, L. Spinu, D. H. Kim and D. Talbayev, *J. Appl. Phys.*, 2013, **114**, 103704.
- 23 T. Tynell, I. Terasaki, H. Yamauchi and M. Karppinen, *J. Mater. Chem. A*, 2013, **1**, 13619 – 13624.
- 24 T. Tynell, A. Giri, J. Gaskins, P. E. Hopkins, P. Mele, K. Miyazaki and M. Karppinen, *J. Mater. Chem. A*, 2014, **2**, 12150 – 12152.
- 25 J.-P. Niemelä, A. Giri, P. E. Hopkins and M. Karppinen, *J. Mater. Chem. A*, 2015, **3**, 11527.
- 26 G. S. Hammond, D. C. Nonhebel and C.-H. S. Wu, *Inorg. Chem.*, 1963, **2**, 73 – 76.
- 27 T. S. Tripathi, M. Bala and K. Asokan, *Rev. Sci. Instrum.*, 2014, **85**, 085115.
- 28 K. Klepper, O. Nilsen and H. Fjellvag, *Thin Solid Films*, 2007, **515**, 7772 – 7781.
- 29 K. Uusi-Esko and M. Karppinen, *Chemistry of Materials*, 2011, **23**, 1835–1840.
- 30 E. Ahvenniemi, M. Matvejeff and M. Karppinen, *Dalton Trans.*, 2015, **44**, 8001–8006.
- 31 R. Huang and A. H. Kitai, *Journal of Electronic Materials*, 1993, **22**, 215–220.
- 32 M. Coll, J. M. M. Moreno, J. Gazquez, K. Nielsch, X. Obradors and T. Puig, *Advanced Functional Materials*, 2014, **24**, 5368–5374.
- 33 X. Qin, H. Sun and F. Zaera, *J. Vac. Sci. Technol. A*, 2012, **30**, 01A112.
- 34 N. Reeves-McLaren, J. Sharp, H. Beltrán-Mir, W. M. Rainforth and A. R. West, *Proceedings of the Royal Society A: Mathematical, Physical and Engineering Science*, 2016, **472**, 20140991.
- 35 W. Wunderlich, *ACSE*, 2013, **2**, 9 – 15.
- 36 W. L. Roth, *J. Phys. Chem. Solids*, 1964, **25**, 1 – 10.
- 37 N. K. Appandairajan and J. Gopalakrishnan, *Proc. Indian Acad. Sci.*, 1978, **87A**, 115 – 120.
- 38 H. M. Rietveld, *J. Appl. Cryst.*, 1969, **2**, 65 – 71.
- 39 T. Goryczka, G. Dercz, L. Pajak and E. Lagiewka, *Solid State Phenom.*, 2007, **130**, 281 – 286.
- 40 Z. Wang, J. Yin and Y. Jiang, *Micron*, 2000, **31**, 571 – 680.
- 41 W. Waddington, P. Rez, I. P. Grant and C. J. Humphreys, *Phys. Rev. B*, 1986, **34**, 1467 – 1473.
- 42 M. N. Iliev, P. Silwal, B. Loukya, R. Datta, D. H. Kim, N. D. Todorov, N. Pachauri and A. Gupta, *J. Appl. Phys.*, 2013, **114**, 033514.
- 43 V. G. Hadjiev, M. N. Iliev and I. V. Vergilov, *J. Phys. C: Solid State Phys.*, 1988, **21**, L199 – L201.
- 44 C. F. Windisch, Jr., G. J. Exarhos and R. R. Owings, *J. Appl. Phys.*, 2004, **95**, 5435 – 5442.
- 45 J. D. Perkins, T. R. Paudel, A. Zakutayev, P. F. Ndione, P. A. Parilla, D. L. Young, S. Lany, D. S. Ginley, A. Zunger, N. H. Perry, Y. Tang, M. Grayson, T. O. Mason, J. S. Bettinger, Y. Shi and M. F. Toney, *Phys. Rev. B*, 2011, **84**, 205207.

- 46 R. D. Shannon, *Acta Cryst.*, 1976, **A32**, 751 – 767.
- 47 I. G. Austin and N. F. Mott, *Adv. Phys.*, 1969, **18**, 41 – 102.
- 48 N. F. Mott, *J. Non-Cryst. Solids*, 1968, **1**, 1 – 17.
- 49 R. Schmidt, A. Basu, A. W. Brinkman, Z. Klusek and P. K. Datta, *Applied Physics Letters*, 2005, **86**, 073501.
- 50 A. L. Efros and B. I. Shklovskii, *Journal of Physics C: Solid State Physics*, 1975, **8**, L49–L51.
- 51 T. M. Mok and S. K. O'Leary, *J. Appl. Phys.*, 2007, **102**, 113525.
- 52 L. Qiao, H. Y. Xiao, H. M. Meyer, J. N. Sun, C. M. Rouleau, A. A. Puzdov, D. B. Geohegan, I. N. Ivanov, M. Yoon, W. J. Weber and M. D. Biegalski, *J. Mater. Chem. C*, 2013, **1**, 4628 – 4633.
- 53 K. Dileep, B. Loukya, P. Silwal, A. Gupta and R. Datta, *J. Phys. D: Appl. Phys.*, 2014, **47**, 405001.
- 54 P. D. Battle, A. K. Cheetham and J. B. Goodenough, *Mater. Res. Bull.*, 1979, **14**, 1013 – 1024.
- 55 J. F. Marco, J. R. Gancedo, M. Gracia, J. L. Gautier, E. I. Rios, H. M. Palmer, C. Greaves and F. J. Berry, *J. Mater. Chem.*, 2001, **11**, 3087 – 3093.
- 56 S. Holgersson and A. Karlsson, *Z. anorg. allg. Chem.*, 1929, **183**, 384 – 394.
- 57 O. Knop, K. I. G. Reid, Sutarno and Y. Nakagawa, *Can. J. Chem.*, 1968, **46**, 3463 – 3476.
- 58 S. Blanco-Canosa, F. Rivadulla, V. Pardo, D. Baldomir, J.-S. Zhou, M. García-Hernández, M. A. López-Quintela, J. Rivas and J. B. Goodenough, *Physical Review Letters*, 2007, **99**, year.
- 59 J. B. Goodenough, *Magnetism and the Chemical Bond*, 1963.